A Micro-Fabricated Linear Array of Electrospray Emitters for Thruster Applications

Luis Fernando Velásquez-García, Akintunde Ibitayo Akinwande, *Member, IEEE*, and Manuel Martínez-Sánchez

***Abstract*—This paper reports the design, fabrication, and experimental characterization of an internally fed linear array of electrospray emitters intended for space propulsion applications. The engine uses doped formamide as propellant and operates in the single-Taylor-cone droplet emission regime. The engine implements the concept of hydraulic and electrodynamic flow rate matching to achieve electrical control. The engine uses a set of meso-scaled silicon deflection springs to assemble the hydraulics to the electrodes, allowing to decouple the corresponding process flows. The micro-fabrication of the engine is described and novel technologies that were developed are reported. Experimental results that demonstrate cumulative uniform and steady operation are provided. Current–flowrate characteristics of the engine are in agreement with a reduced-order model. Experimental data demonstrating the low divergence of electrospray emitter arrays operated in the single Taylor Cone is in qualitative agreement with a reduced-order mode that assumes the absence of a thermalized tail in the plume. [1420]**

***Index Terms*—Electrical flow control, electrospray array, propulsion, spring deflection system, three-dimensional (3-D).**

I. Introduction

ELECTROSPRAY thrusters are electrostatic accelerators of charged particles. These particles could be charged droplets, solvated ions, or a mix of them. The exit stream is neutralized either by bipolar operation of the engine (modulation in space to achieve overall neutrality) or by a downstream electron stream (positively charged exit stream). Fig. 1 shows a schematic of an emitter unit, which is part of an internal pressure-fed electrospray thruster array that works in the single-cone, droplet emission mode. In Fig. 1, the engine propellant plenum has stored propellant at a static pressure P_o. This propellant flows through a hydraulic system to the emitters. The hydraulic system can be modeled as a hydraulic impedance operating across a pressure difference. Two lengths can be used to describe the hydraulic impedance: the hydraulic diameter L_c and the axial channel length L. At the end of the hydraulic system, there is an opening to the engine exterior,

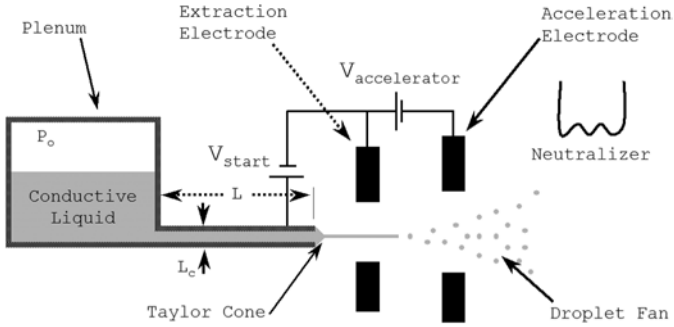

Fig. 1. Schematic of an internally fed electrospray emitter.

i.e., an emitter. There is a set of two electrodes in front of the spout, the first one intended to extract charged particles from the emitter (extractor), and the second electrode to accelerate the particles to the desired specific impulse (accelerator). The specific impulse $I_{\rm sp}$ is defined as

$$I_{\rm sp} = \frac{F}{\dot{m} \cdot g} \cong \frac{c}{g} \tag{1}$$

where F is the thrust, $\dot{m}$ is the mass flowrate, g is the gravity's constant, and c is the exit stream velocity. In order to maintain the engine charge neutrality, a neutralizer is placed downstream to provide particles with opposite charge that will mix with the exit stream. The voltage between the extractor and the emitter should be large enough to produce a single jet at each emitter, but smaller than the voltage that would make the meniscus emit multiple jets.

The existence of a bias voltage between the meniscus and the extractor creates an electric field in the space between, in particular on the meniscus surface. The electric field will produce electrostatic suction on the meniscus surface. The surface tension of the liquid tends to counteract the effect of the electrostatic suction. For sufficiently small bias voltages, the perturbation of the equilibrium shape remains small. If the electric field is larger than a certain threshold, the surface tension effects can no longer counteract the electrostatic pulling and, therefore, the meniscus snaps into a conic shape called a Taylor cone. The Taylor cone becomes the equilibrium shape between the acting electrostatic pressure and the surface tension reaction. To first order, the cone semi-angle has a universal value of 49.3° [1].

The normal electric field E_n acting on the propellant free surface at the emitter tips can be described as [2]

$$E_n = \psi \cdot \frac{V}{\sqrt{L_{c,o} \cdot L_c}} \tag{2}$$

Manuscript received September 4, 2004; revised November 15, 2005. This work was supported by the Air Force Office of Scientific Research (AFOSR) under Grant F49620-01-1-0398. Subject Editor Y.-C. Tai.

L. F. Velásquez-García is with the Department of Aeronautics and Astronautics and the Department of Electrical Engineering and Computer Science, Massachusetts Institute of Technology, Cambridge, MA 02139 USA (e-mail: lfvelasq@mit.edu).

A. I. Akinwande is with the Department of Electrical Engineering and Computer Science, Massachusetts Institute of Technology, Cambridge, MA 02139 USA (e-mail: akinwand@mtl.mit.edu).

M. Martínez-Sánchez is with the Department of Aeronautics and Astronautics, Massachusetts Institute of Technology, Cambridge, MA 02139 USA (e-mail: mmart@mit.edu).

Digital Object Identifier 10.1109/JMEMS.2006.879707

where V is the applied voltage, L_c is the inner diameter (cone size), $L_{c,o}$ is the outer diameter, and ψ is a dimensionless factor. Therefore, the threshold electric field $E_{n,\mathrm{start}}$ obeys the relationship

$$\frac{\varepsilon_o}{2} \cdot E_{n,\mathrm{start}}^2 > \beta \cdot \frac{\gamma}{L_c} \tag{3}$$

where ε_o is the electrical permittivity of free space, γ is the surface tension of the liquid, and β is a dimensionless factor. A more elaborated reduced-order model predicts that the threshold voltage difference V_{start} is given approximately by the expression [3]

$$V_{\mathrm{start}} = \sqrt{\frac{\gamma \cdot L_{c,o}}{\varepsilon_o}} \ln\left[\frac{4G}{\sqrt{L_c \cdot L_{c,o}}}\right] \tag{4}$$

where G is the emitter-to-extractor separation, and $4G > (L_c.L_{c,o})^{0.5}$.

The total current emitted by a Taylor cone as a droplet fan issuing from the cone apex is [4]

$$I = f(\varepsilon)\sqrt{\frac{\gamma \cdot K \cdot Q}{\varepsilon}} \tag{5}$$

where ε is the relative electrical permittivity, γ is the surface tension, K is the electrical conductivity, Q is the volumetric flowrate, and $f(\varepsilon)$ is a dimensionless function of the electrical permittivity. For ε values larger than 40, the function $f(\varepsilon)$ tends to a limit value experimentally found to be near 20. Equation (5) is independent of voltage, but it applies only as long as the single cone jet regime holds, which is in a narrow voltage range near the start-up voltage [5]. Using (5), for an array of spouts emitting uniformly, one can readily show that the relationship between the total current I_{tot} and the total flowrate Q_{tot} is given by

$$I_{\mathrm{tot}} = f(\varepsilon)\sqrt{\frac{\gamma \cdot K \cdot Q_{\mathrm{tot}}}{\varepsilon}} \cdot \sqrt{n} \tag{6}$$

where n is the total number of emitters of the array. The specific charge δ of the emitted species is defined as

$$\delta = \frac{q}{m} = \frac{f(\varepsilon)}{\rho}\sqrt{\frac{\gamma \cdot K}{\varepsilon \cdot Q}} \tag{7}$$

where q is the particle charge, m its mass, and ρ is the propellant density. In a colloid thruster, it is desired to increase as much as possible the specific charge because this implies larger specific impulse values for a fixed potential drop V

$$I_{\mathrm{sp}} = \frac{\mathrm{Thrust}}{\mathrm{Weight\ Flowrate}} = \frac{1}{g}\sqrt{2\frac{q}{m}V}. \tag{8}$$

Therefore, the engine should use as little flowrate as possible, down to $Q_{\min}$, the minimum flowrate at which steady-sate operation can be sustained [4]

$$Q_{\min} = \eta_{\min}^2 \frac{\gamma \cdot \varepsilon \cdot \varepsilon_o}{\rho \cdot K} \tag{9}$$

where $\eta_{\min}$ is the minimum value that the dimensionless parameter η can get for stable Taylor-cone operation. The dimensionless parameter η is the square root of the ratio between inertial and capillary forces evaluated at the point where the electric field is maximum (near the cone apex). Experimentally, it is known that the minimum value for η is about 1.

A reduced-order model proposed by Lozano [6] predicts that the semi-angle divergence θ_B of the fan of formamide droplets is given by

$$\theta_B \cong \arctan\left[26.73 \cdot \frac{\eta^{3/4}}{K^{1/4} \cdot V^{3/4}}\right] \tag{10}$$

where η is the dimensionless flowrate, K is the electrical conductivity of the liquid, and V is the extraction voltage.

During the 1960s and 1970s, there was a substantial amount of work done in the development of electrospray thrusters that operated in the highly stressed (multiple cone) regime, both using needles and slit geometries [7]–[9]. These engines had low emitter density and had rather large beam divergence because of the mutual repulsion among the low-speed part of the multiple jets.

Since the new advances in electrospray technology that occurred in the late 1980s [10], the field of electrospray propulsion has experienced a renaissance, specifically aiming to provide efficient high-tunable precision low-thrust engines for micro-satellites and high-accuracy astrophysics missions [11]. Several attempts to develop micro-fabricated electrospray thruster technology have been made in the last few years by other teams [12]–[14]. Also, substantial work has been done in implementing disposable, nongated, micro-fabricated electrospray sources for mass spectrometry applications [15]. Recent work on electrospray technology in our laboratory has focused on dense arrays of electrospray emitters for space propulsion applications [3], [16]–[18]. The linear array reported in this paper, which is one of the technology developments of our research program, will be briefly described in Section II.

II. Linear Array

Fig. 2 shows a set of pictures of the linear array and a 3-D computer model of an exploded engine. The engine hydraulic system is composed of one plenum, 12 manifolds, and 240 emitters. The hydraulic system opens to the exterior at the propellant plenum inlet and at the emitter tips. The emitters are sharpened to reduce the startup voltage. The device requires approximately 2000 V to get activated. The engine has implemented electrical flow control, as will be described later in this section. The electrodes are micro-fabricated with conductive paths made of tungsten and electrical insulation provided by vacuum

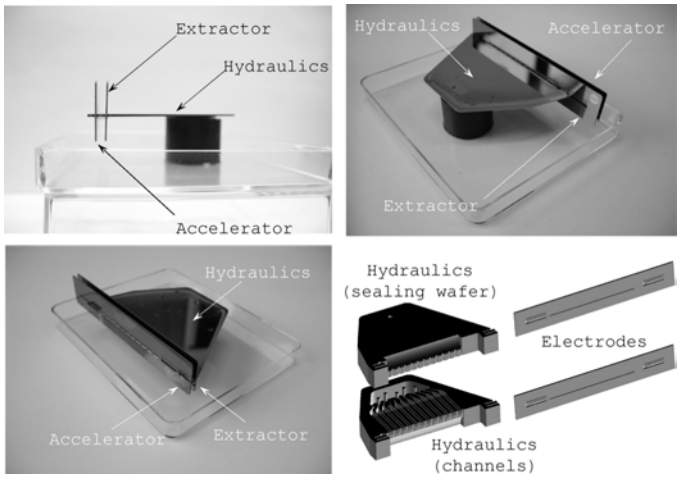

Fig. 2. Selected views of a micro-fabricated linear array and a 3-D model of an exploded device. The extractor electrode pad and the plenum propellant inlet are visible on the upper right picture.

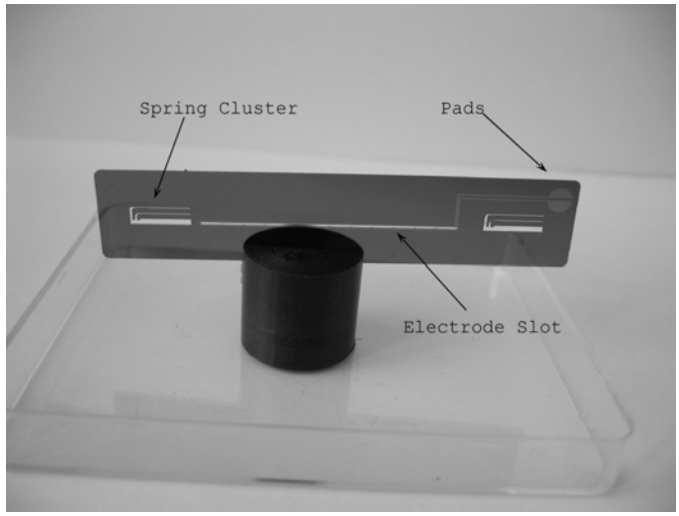

Fig. 3. Micro-fabricated electrode, part of the electrospray linear array.

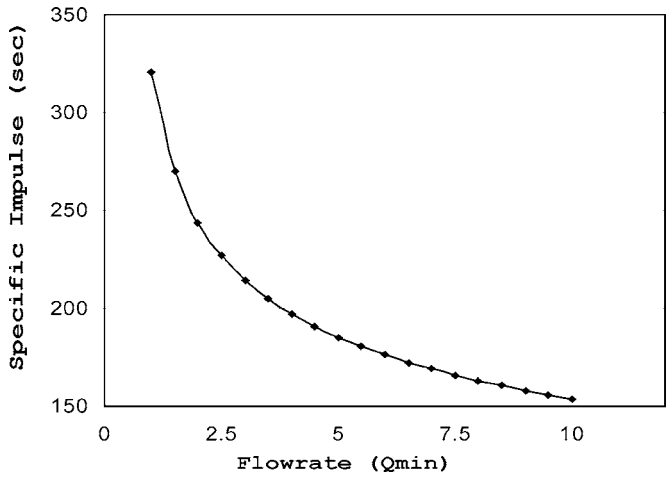

Fig. 4. Expected performance for the linear array: specific impulse versus flowrate.

gaps that are 350 μm long (shortest distance from an emitter tip to the electrode conductive path) and 10-μm-thick plasma-enhanced chemical vapor deposited (PECVD) silicon oxide. The engine body is covered with PECVD oxide to complete the device's electrical insulation. The engine is its own package. To be testable, the engine only requires a micro-fluidic port connected to the engine propellant inlet and the appropriate electrode pad wiring (the propellant plenum is used as ground). Each electrode has a slit that becomes wider in the direction of emission (electrode expansion). The electrode expansion is intended to minimize the possibility of particle interception by the electrodes due to the beam divergence. Each electrode is physically supported by two post-like structures that are placed at either end of the emitter tip array. This architecture provides good electrical insulation because the electrodes touch the engine frame only at a few points, away from the emitters (for practical purposes, the electrodes are hovering on top of the emitters, with no physical connection). The electrodes are hand-assembled to the engine hydraulics using a novel technique that relies on sets of meso-scaled micro-fabricated springs. [19] These springs are patterned using deep reactive ion etching (DRIE) as part of the process flows of the hydraulics and the electrodes. The spring dimensions are such that allow hand-assembling the engine with the required precision (the maximum misalignment value was set at 60 μm for an electrode with an opening 300 μm, wide, separated 250 μm from the emitter tips).

The emitter-to-emitter separation is 130 μm and the hydraulic diameter is 12 μm. The engine uses highly doped formamide as a propellant, with electrical conductivity in the 0.3–3.0-S/m range. The formamide is doped with ionic salts. We have used both NaI and LiCl as doping salts because we have found experimentally that they can be added to the formamide at room temperature in such amounts that they can increase the electrical conductivity of the formamide to levels of the order of 1 S/m without precipitating. To the best of our knowledge, either salt can be used for our application. The conductivity of the propellants used with the engine was determined using a Jenway conductivity meter 4320.

Fig. 3 shows one of the electrodes used in the linear array. To avoid excessive electrode deflection of the electrode because of the slot expansion in the direction of emission, the electrode has a set of ribs that enhance its stiffness. A conductive path made of W/Ti surrounds the electrode slot. This conductive path is separated from the silicon substrate by a thick layer of thermal + PECVD silicon oxide. The conductive path has two pads for electrical contact. The electrode has two clusters of displacement springs that are used to assemble the electrode to the engine hydraulics with the required precision. These spring sets clamp into the post-like structures that the hydraulic subsystem has.

Figs. 4–6 illustrate the specific impulse, propulsive power, and expected thrust for the linear array when using a total potential drop of 5000 V and doped formamide with an electrical conductivity equal to 0.6 S/m as propellant. In these estimations, the following is assumed: small divergence of the beam, no electrode particle interception (optimized optics), a bias voltage between the extractor and the emitter such that a single Taylor cone is formed on each meniscus (the rest of the potential drop

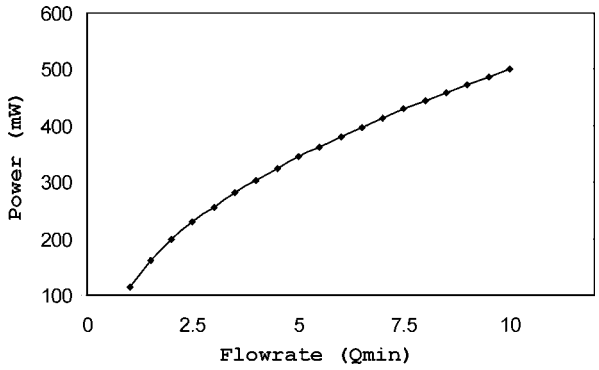

Fig. 5. Expected performance for the linear array: propulsive power versus flowrate.

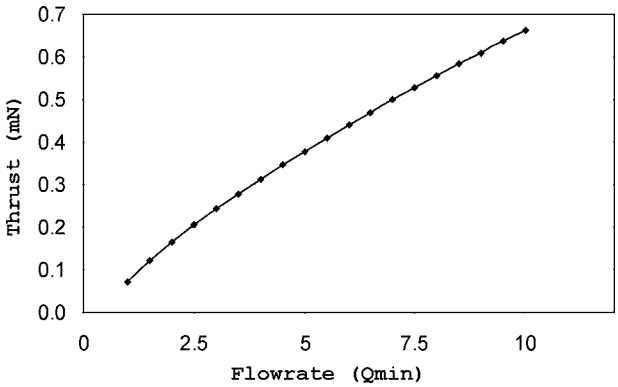

Fig. 6. Expected performance for the linear array: thrust versus flowrate.

is set between the extractor and the accelerator), and evaporation losses have been omitted (they should be smaller than 1% given the emitter size [3]). The abscissa is given in multiples of $Q_{\min}$ for the 240 emitters: 2.05×10^{-11} m^3/s. The engine can provide specific impulse in the 150–350-s range, and trust in the 50–650-μN range, while consuming power in the 100–500-mW range. Therefore, the strength of this engine is not its specific impulse, but its potential for use in highly tunable time-critical low-thrust missions such as orbital transfer for micro-satellites. The linear array is consequent with this application because it integrates in a single chip the hydraulic impedance, emitter head, and electrodes; the lack of need for an active pump (as will be explained later in the text, the engine is electrically controlled using a constant pressure signal) also is favorable for a system with large constraints in weight, volume, and power, as is the case of a micro-satellite.

The concept behind the electrical control of the linear array can be summarized in the following points, and it is applicable to many propellants/engine architectures.

- There is a pressure difference between the engine propellant plenum and the external atmosphere surrounding the engine. This pressure difference is used to feed the propellant to the emitters. To first order, the pressure outside the emitters is zero, thus making the pressure delta equal to P_o.
- The pressure difference between the plenum and the exterior is such that, given the hydraulic impedance of the system, it provides a flowrate that falls within the range of flowrates that can be steadily pumped by the Taylor cones when the electrodes are activated. This is a rather wide range of flowrates, experimentally known to be from $Q_{\min}(\eta$ is about 1) to 100 $Q_{\min}(\eta$ is about 10) [4].
- The pressure difference between the engine plenum and the outside is smaller than the maximum pressure that the meniscus at the emitters tips can withstand before breaking/producing flow (P^*). Therefore, no flow is possible unless the extractor electrodes are activated. The fraction of the maximum surface tension pressure P^* that is actually applied at the engine tank is arbitrarily defined. Fractions closer to unity will produce a meniscus with a smaller radius of curvature.
- The extra pressure needed to break the meniscus and produce flow is externally supplied as electrostatic pressure by the extractor electrode. The applied voltage between the emitters and the extractor electrode will induce charge at the surface of the meniscus that will set an electric field at the meniscus surface, responsible for the electric suction at the interface that will eventually generate the flow.
- Once the fraction of the maximum static pressure that can be applied to the engine has been selected, the channel hydraulic diameter is obtained by equating the hydraulic loss to the fraction of the maximum meniscus capillary pressure. This flowrate matching implies for most electrolytes a large length-to-hydraulic diameter ratio, i.e., large hydraulic impedance.
- High L-to-L_c ratios are obtained, while having the cross section dimensionally controlled, by carving the feed channels along the top surface of the wafer.
- A small hydraulic diameter implies a smaller start-up voltage, as predicted by (4).

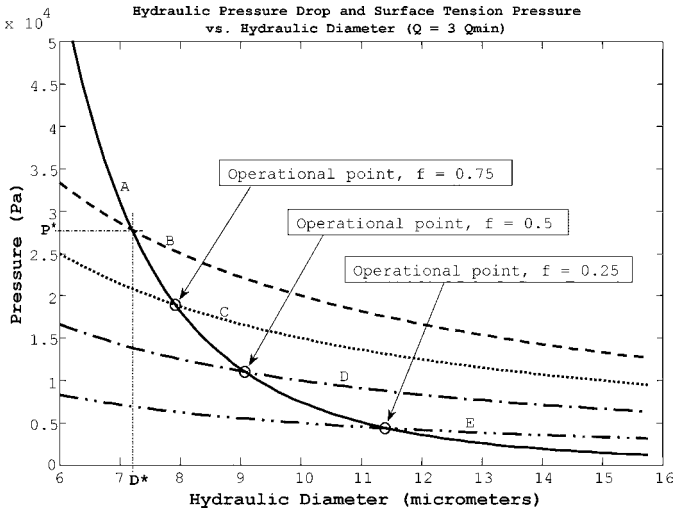

Fig. 7. Pressure difference and surface tension pressure versus L_c for a fixed flowrate.

Fig. 7 illustrates the hydraulic behavior of our engine concept using doped formamide with $K = 2.3\ \mathrm{S/m}$. This figure shows the propellant plenum static pressure (A) and several percentages of the maximum reservoir pressure before producing flow [100% (B), 75% (C), 50% (D), 25% (E)], all versus hydraulic diameter for a fixed flow rate—three times the minimum flow rate. The channel axial length is also fixed at 15 mm. In order to

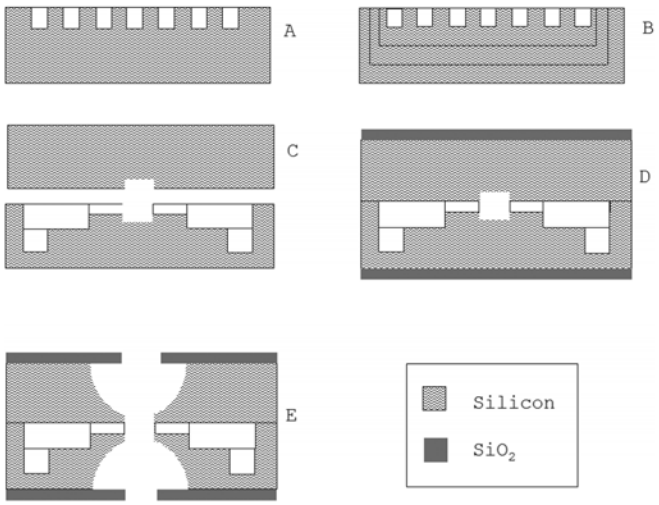

Fig. 8. Process flow of the hydraulic system. (A) Definition of flow channels. (B) Definition of manifolds and plenum. (C) Oxide growth and spout frontal area definition. (D) Wafer bonding and SiO_2 deposition. (E) Spout sharpening and engine release. In (C)–(E), two engines are shown facing each other.

electrically control the engine, the diameter L_c should be larger than D^*, which is the hydraulic diameter value at the intercept between the line of 100% surface tension and the pressure line. The particular L-to-L_c ratio is given, for an emitter with constant circular cross section, by

$$\frac{L}{L_c} = \left[\frac{0.1326 \cdot \gamma \cdot f \cdot L^2}{Q \cdot \mu}\right]^{1/3} \tag{11}$$

where γ is the surface tension of the liquid, f is the fraction of the maximum pressure that the meniscus can withstand before breaking, Q is the flowrate through the emitter, and μ is the liquid viscosity. Graphically, this L_c is at the intersection of the curve (A) with the curve whose fraction f was chosen. The intersection of the curves (A) and (B) define D^* and P^*.

To reach the desired I_{sp}, a second electrode, the accelerator, is placed with a bias voltage with respect to the extractor. The purpose of a second electrode is to maintain a sufficiently low extraction voltage to assure that just one Taylor cone is produced in each emitter, regardless of the voltage needed to reach the I_{sp}/thrust goal.

III. Micro-Fabrication of the Colloid Thruster Linear Array

The engine uses four silicon substrates, two for the hydraulics and one for each electrode. The fabrication of the linear colloid thruster array is composed of two process flows: one for the hydraulics and one for the electrodes. In both cases, 6-in, Si $p\langle 100\rangle$ double-side polished, lightly boron doped, 375-μm-thick substrates are used. The engine is entirely patterned using plasma etching, both reactive ion etching (RIE) and DRIE.

A. Process Flow to Produce the Hydraulic System

The fabrication of the hydraulic system required seven optical masks and 12 photolithographic processes. The abbreviated process flow is shown in Fig. 8, and a short description is given below.

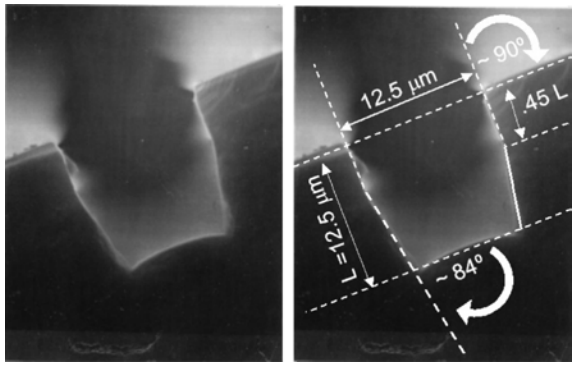

Fig. 9. Cross section of one of the channels with its corresponding metrology. The remaining SiO_2 etching mask is still present.

The process starts with the definition of the alignment marks on both sides of the double-sided polished 6-in wafers. A novel chlorine-based plasma recipe, which produced *black silicon* [20], was used to define the alignment marks in a LAM 490B plasma etcher. The use of a *black silicon* recipe allows excellent alignment during subsequent lithographic steps, even though several films that are tens of microns have been deposited on the wafer substrate.

The second step in the process is the definition of the flow channels in the top surface of the bottom wafer. A novel anisotropic chlorine-based plasma recipe was developed to uniformly pattern square channels 12 μm wide and 15 mm long, with dimensional variation smaller than 2% across the whole wafer, using a LAM 490B plasma etcher. The impedance of the flow circuit is strongly influenced by the nonuniformities in the patterning, and, therefore, close dimensional control was required. Fig. 9 shows a series of pictures that characterize the flow channel formation. We intended to etch channels with square cross section to make the channel geometry robust to misalignments when wafer bonding the substrates that constitute the hydraulics.

The third step in the process is the definition of the engine manifolds and propellant plenum on the top surface of the bottom wafer. A PR/SiO_2 nested mask and a series of DRIE without passivation phase were used to define these features, in order to avoid stress concentrators and have a smooth hydraulic transition between the tank, manifolds, and channels.

The fourth step in the process is the growth of a thin layer of thermal silicon oxide on both wafers. This film has two functions: etch stop for subsequent plasma etching steps and wettability enhancer of the engine interior with respect to the propellant.

The next step is the definition of the emitters front surfaces using a shallow anisotropic etch. Then, top and bottom wafers are fusion bonded. Fig. 10 shows selected cross sections of the bonded wafer pair.

The following step comprises the deposition of thick layers of PECVD silicon oxide on both sides of the wafer pair. Thick silicon oxide films are needed to mask the final silicon etching steps of the hydraulic system because of the etch depth involved and concerns about the etching selectivity of the plasma recipes.

The process continues with the definition of the springs and the remaining engine emitter features on the silicon oxide films. The silicon oxide films are anisotropically patterned with a novel plasma recipe using C_2F_6 and CHF_3 in an Applied

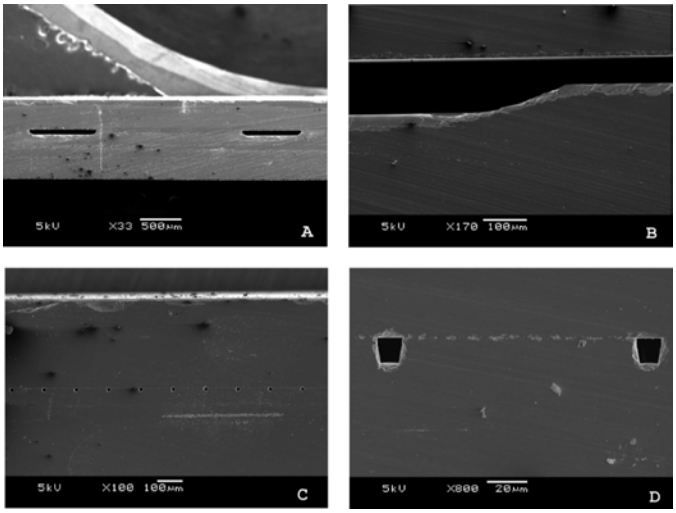

Fig. 10. Selected cross sections of the bonded wafer pair. (A) Two manifolds in cross section. (B) Transition between plenum and a manifold. (C) Cross section of a set of channels. (D) Cross section of adjacent channels.

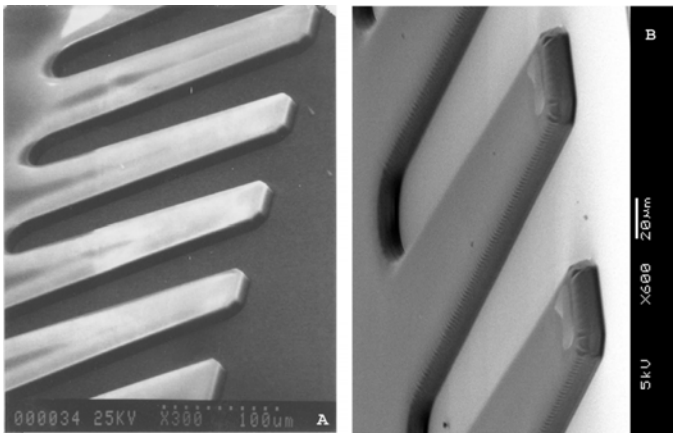

Fig. 11. SEM pictures of a thick SiO_2 layer patterned to generate the spout sharpening using (A) AME Centura 5300 and (B) AME P 5000.

Materials Centura 5300 high-density plasma etcher or an Applied Materials P 5000 magnetically coupled R. F. plasma etcher. As pointed out in the previous section, the springs are used to later hand-assemble the hydraulics with the electrodes. Fig. 11 shows the patterning of the thick silicon oxide layer in the section that eventually becomes the engine emitters.

Then, the springs are covered with photoresist to protect them from intermediate processing. After this, the engines are released from the bonded substrate, while sharpening their emitters, by using a nonpassivated DRIE step.

The process concludes with the definition of the springs in the silicon wafer stack using DRIE and coating the engine exterior with a Teflon film. The DRIE step uses a pressure-controlled plasma etching recipe that results in uniform vertical sidewalls, and the oxide mask on top of the emitters acted as an umbrella to protect the emitters from unwanted etching. The Teflon film is intended to address wettability issues, and its thickness was experimentally found to be a fraction of a micron. The coating was carried out using the passivation cycled of a dedicated DRIE recipe.

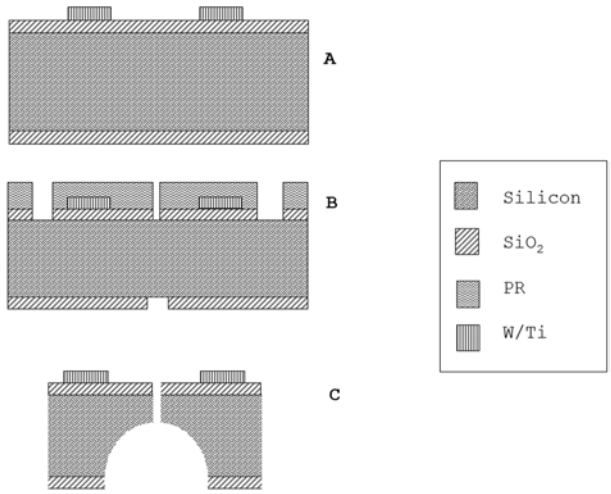

Fig. 12. Process flow of the electrodes of the linear array. (A) Definition of conductive paths. (B) Silicon oxide etching masks patterning. (C) Electrode slot patterning and electrode release.

B. Process Flow to Produce the Electrodes

To fabricate the electrodes, four optical masks, five photolithographic processes, and more than 60 fabrication processes are required. The electrode has a conductive path made of *W/Ti* on top of a 10-μm-thick PECVD silicon oxide layer. Fig. 12 illustrates the abbreviated fabrication flow, and a short description is given below.

The process starts with the definition of the alignment marks on both sides of the substrate. As in the case of the engine hydraulics, black silicon is also used to pattern these features.

Then, the process continues with the growth and deposition of SiO_2 on both surfaces. A 1-μm-thick layer of SiO_2 is thermally grown, followed by a 9-μm-thick PECVD SiO_2 film using a Novellus Concept One dielectric plasma deposition system. The silicon oxide layers provide electrical insulation.

Third, the process continues with the deposition of thin layers of *Ti* and *W* on the top surface, using an electron-beam physical vapor deposition (PVD) system. *Ti* is the adhesion layer for the *W* electrode. *W* was chosen as the electrode material because of its sputter resistance.

The following step in the process is the definition of the electrodes. *W* was patterned using a SF_6-based plasma chemistry while *Ti* was patterned a Cl_2-based plasma chemistry, using a LAM Rainbow 9600 metal etch system. Fig. 13 shows a plasma-patterned electrode conductive path.

Then, backside and front-side oxide layers are patterned. Provision was made for widening the electrode slot on the exit side (bottom surface) to prevent particle interception. A set of ribs was added to enhance the stiffness of the electrode. Also included, but patterned on the front side, are electrode slots and the springs that enable the assembly of the electrodes to the hydraulics.

The process is completed with DRIE of the wafer front and backside. The first etch uses a nonpassivated DRIE cycle to widen the electrode slots. The second DRIE step defines the electrode slots and the springs; in the second DRIE the electrodes are also released. Fig. 14 shows selected cross sections

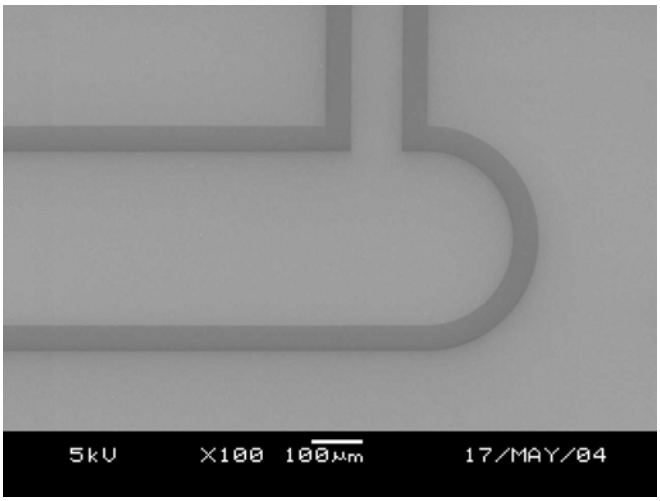

Fig. 13. Detail of a plasma-patterned conductive line. The electrode slot is patterned inside the loop.

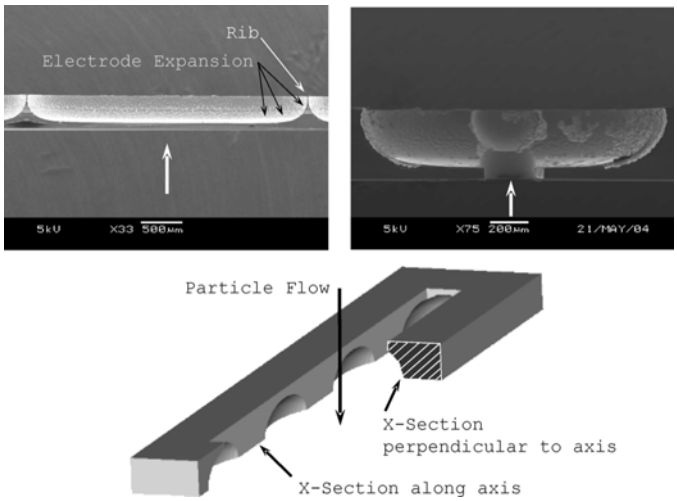

Fig. 14. Electrode cross sections. Cross section of the electrode along its axis, showing two of the ribs that enhance the electrode stiffness (upper left); cross section of the electrode perpendicular to its axis, showing the electrode expansion in the direction of the flow—wide arrows (upper right); 3-D model of the electrode illustrating the two cross sections that are shown in the SEMs (bottom).

of a micro-fabricated electrode. A 3-D computer model is also provided in Fig. 14 to better understand the SEMs of the cross sections. Fig. 15 is an exploded view of the micro-fabricated linear array where the different parts that constitute the engine hydraulics and electrodes are shown, with the help of a computer-generated 3-D model.

IV. Experimental Results

A. Electrode Tests

The extractor was first evaluated for electrical breakdown using the testing jig shown in Fig. 16. The test jig consists of a PVC engine fixture and a resistive voltage divider connected in series with the vacuum gap, as shown in Fig. 17. In case of breakdown, the current through the vacuum gap is limited by the larger resistor and monitored by the smaller resistor using a voltmeter. If no breakdown occurs, the voltage drop measured through the smaller resistor should be zero. The engine test setup was inside a vacuum chamber pumped below 10^{-7} torr using two 70-L/s turbo-pumps. Tests were conducted at a pressure of 10^{-7} torr with no propellant present. Then, 2500 V dc was applied between the engine inlet and the electrodes using the electrode pads. No breakdown current was measured by the Fluke 199 Scope Meter in 12 h of breakdown test.

B. Operational Tests of the Engine

Fig. 18 shows the test jig for evaluating the wet operation of the engine, which is fed by a propellant system shown schematically in Fig. 19. The test jig was placed inside a vacuum chamber pumped below 10^{-6} torr using two 7000 L/s crio-pumps. The propellant system that was implemented was inspired on work done by other researchers in electrospray [21]. The propellant system consists of a nitrogen tank, a mechanical pump, a propellant tank, and a supply line. The system uses mainly ultra-torr fittings that allow for easy modification of the propellant supply configuration. In this propellant system, a decoupled two-flow pattern of propellant and gas is set. The nitrogen tank delivers a gas flowrate driven by the pressure difference between the nitrogen tank regulator $P_{\rm gas}$ and the propellant tank $P_{\rm po}$. This flowrate is equal to the flowrate drawn by the mechanical pump via the pressure difference between the propellant tank pressure $P_{\rm po}$ and the pressure at the pump inlet $P_{\rm pump}$. Once the propellant tank pressure is set by the nitrogen flow, the engine will receive propellant at the rate set by the hydraulic impedance of the engine and the propellant inlet tube, and the pressure difference between the propellant tank and the vacuum chamber pressure (this latter pressure is to first order 0). The nitrogen and propellant flows are considered laminar. The pressure losses at the valves (when fully open) and connections are negligible because they scale with the dynamic head of the flows, and the Reynolds number related to either flow is small. Each tube part of the propellant system is described by a hydraulic diameter and an axial length, as shown in Fig. 19. It can be shown from first principles, assuming ideal gas behavior, constant temperature, and average density for the nitrogen flow, that the propellant tank pressure can be approximated as [3]

$$P_{\rm po} = \sqrt{\frac{\left[\frac{D_{\rm gas}^4}{L_{\rm gas}} \cdot \left(\frac{L_{\rm interm}}{D_{\rm interm}^4} + \frac{L_{\rm pump}}{D_{\rm pump}^4}\right)\right]}{1 + \left[\frac{D_{\rm gas}^4}{L_{\rm gas}} \cdot \left(\frac{L_{\rm interm}}{D_{\rm interm}^4} + \frac{L_{\rm pump}}{D_{\rm pump}^4}\right)\right]}} \cdot P_{\rm gas} \qquad (12)$$

where $L_{\rm gas}$ and $D_{\rm gas}$ are the length and internal diameter of the tube that connects the nitrogen tank to the propellant tank, $L_{\rm interm}$ and $D_{\rm interm}$ are the length and internal diameter of one of the two tubes connected in series that communicate the propellant tank to the mechanical pump (it directly attaches to the propellant tank), and $L_{\rm pump}$ and $D_{\rm pump}$ are the length and internal diameter of the other tube connected in series that communicate the propellant tank to the mechanical pump (it directly

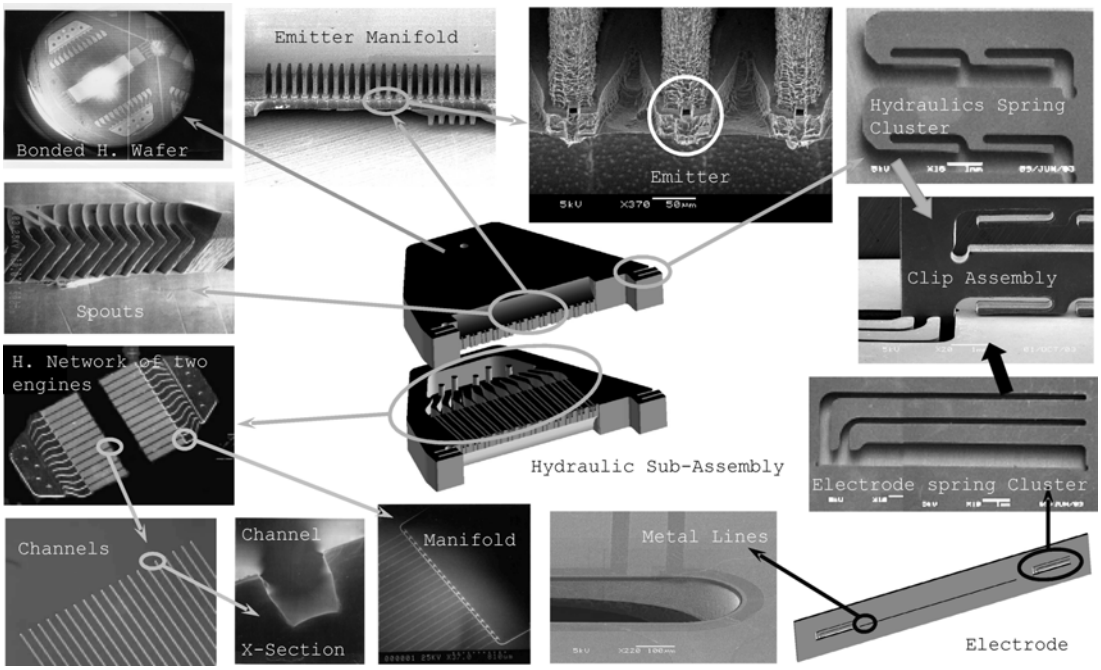

Fig. 15. Linear electrospray thruster array fabrication characterization.

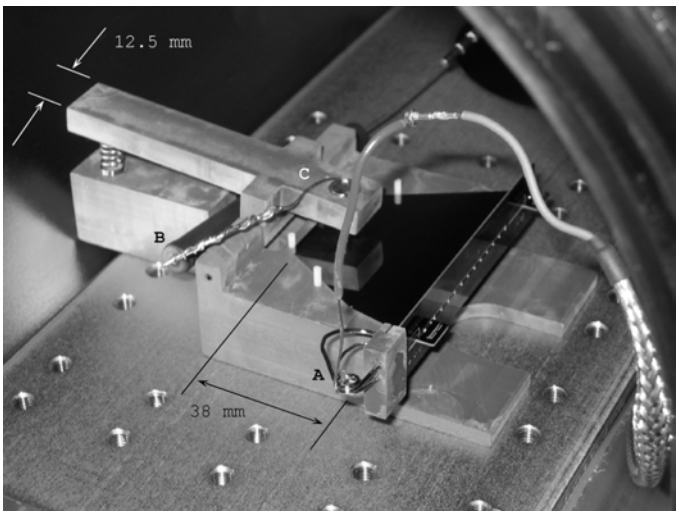

Fig. 16. Picture of the fixture setup used to diagnose the electrode breakdown performance. The engine fixture includes (A) a claw-like appendix enabling electrode contact from both electrode pads. The high-voltage resistor used (B) is visible in the picture. The engine is energized by using the claw-like appendix and the engine body [connected electrically with (C) a probe that compresses the engine].

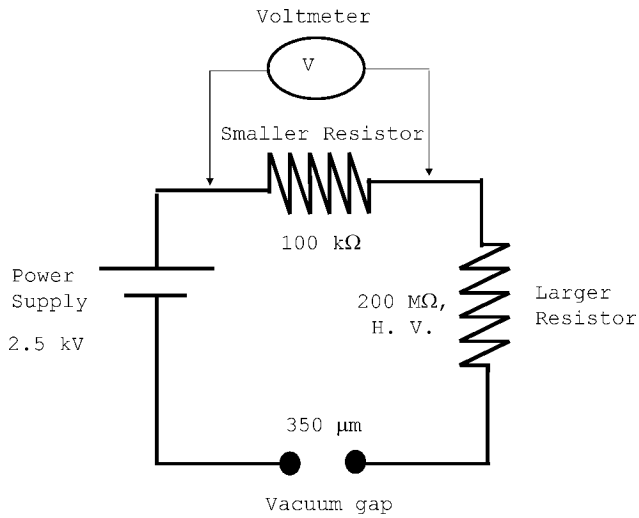

Fig. 17. Schematic of the electrical circuit used to test the electrode breakdown performance.

attaches to the pump inlet). For a fully developed incompressible propellant flow, the pressure at the engine propellant inlet P_o is

$$P_o = \frac{D_{\text{inlet}}^4}{L_{\text{inlet}} \cdot \left[343.66 \cdot \frac{L_C^4}{L} + \frac{D_{\text{inlet}}^4}{L_{\text{inlet}}}\right]} \cdot P_{\text{po}} \qquad (13)$$

where L_{inlet} and D_{inlet} are the length and internal diameter of the tube that directly connects to the engine inlet, and L and L_c are the length and hydraulic diameter of the linear array. Table I summarizes the different dimensions of the constitutive parts of the propellant supply system.

The tank pressure was read using a commercial diaphragm pressure sensor. After the pressure is set to a value that forms a meniscus at the emitter spouts (but that does not produce flow), the emitters receive a bias voltage of about 2000 V dc, leading to the formation of Taylor cones and, thus, propellant emission from the cone apex. A collector electrode is placed at the exit of the engine. The collector was used to bias the emitters. The flowrate coming out of the engine was measured using the well-known method for measuring small flowrates by introducing a bubble in the propellant plenum feed tube [21]. By measuring the time it takes for the bubble to travel a fixed distance, it is

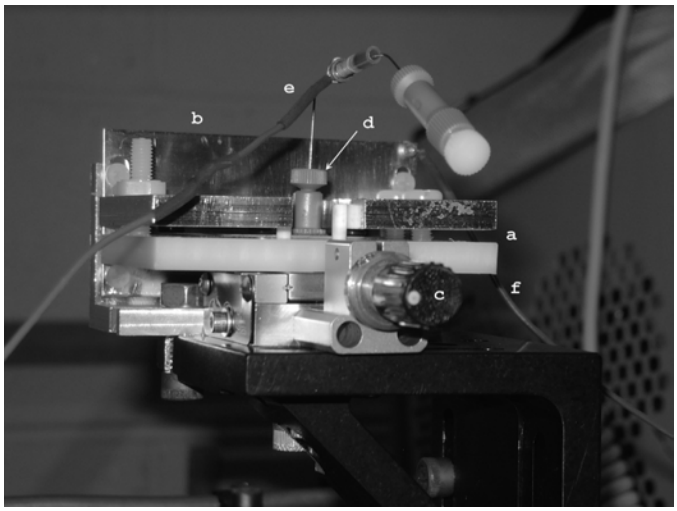

Fig. 18. Linear electrospray thruster array mounted inside the test jig. (a) The engine is inside the gap between two plates. (b) It is facing an external electrode that is separated from the engine spouts (c) using a micrometric screw. (d) The engine has a nanoport (e) connected to a metallic tube that receives an electrical connection. (f) Bias voltage is received using the nanoport connection and a cable connected to the electrode.

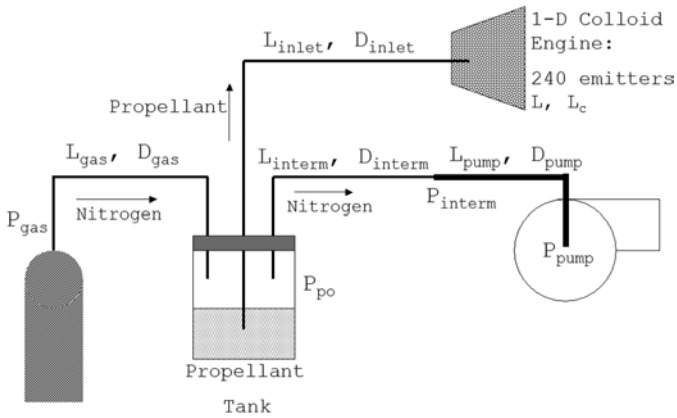

Fig. 19. Schematic of the propellant supply system used to test the linear electrospray thruster array.

TABLE I
HYDRAULIC DIAMETER AND LENGTH OF THE CONSTITUTIVE PARTS OF THE PROPELLANT SYSTEM. THE GAS TUBE CONNECTS THE GAS TANK AND THE PROPELLANT TANK, THE INTERMEDIATE TUBE CONNECTS THE PROPELLANT SUPPLY TO THE PUMP THROUGH THE PUMP TUBE, AND THE INLET TUBE DIRECTLY CONNECTS TO THE ENGINE PROPELLANT INLET

Propellant Supply Part	Hydraulic Diameter (micrometers)	Length (centimeters)
Gas Tube	63.5	100
Intermediate Tube	381	20
Pump Tube	3680	100
Inlet Tube	500	200
Engine	12	1.5

possible to figure out the flowrate if the internal diameter of the tube is known.

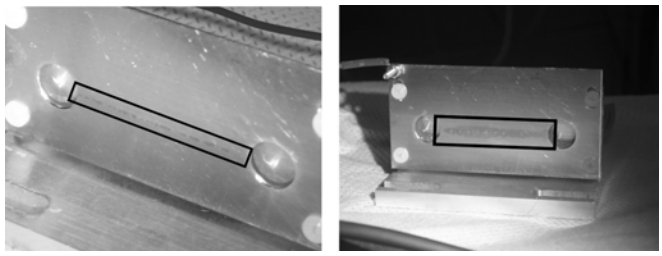

Fig. 20. Impacts from the linear electrospray thruster array on a collector from two different tests/engines.

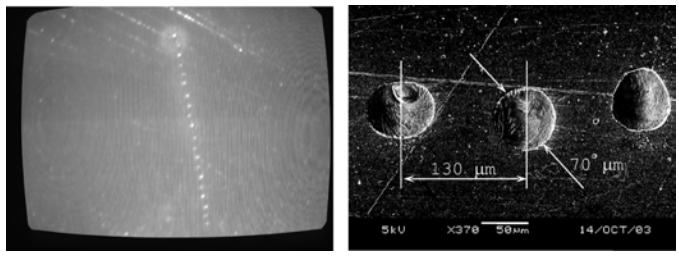

Fig. 21. Fine imprints from a manifold and zoom of the impacts. Collector separation was 250 μm.

C. Electrical Control Tests

The concept of electrical control proposed in this paper was experimentally verified by sequentially turning on and off the power supply while having at the engine plenum less pressure than what the meniscus can resist. This was done for two engines, using formamide with an electrical conductivity of 0.3 Si/m. Emission was verified by measuring the current using the collector. The pressure was not varied during the experiment. No leak was detected by optical inspection of the test stage or the engine. SEM inspection of the engines around the spouts did not show propellant traces away from the spout exits. When propellants with electrical conductivities equal to 2.9 and 0.612 Si/m were used, then leaks near the spouts were detected by visual inspection. In all cases, after cleaning the engine exterior and leaving the engines inside sealed beakers for days, it was verified that the leak was not a product of bad wafer bonding: there is strong evidence that the propellant came out from the engine only through the spouts and that the spills were produced by propellant bursts from the emitters because of wettability problems between the engine interior and the propellant. These wettability problems will be further discussed in a following section.

D. Cummulative Uniformity and Plume Divergence Measurements

Fig. 20 shows pictures of imprints on an external collector electrode made by the exit stream of 240 electrospray emitters of the engine, after a long run (a couple of hours) is performed, using NaI-doped formamide with electrical conductivity equal to 0.3 S/m.

Fig. 21 is a magnified view of the imprints made by the exit stream of a single manifold on a collector electrode. The left-hand picture in Fig. 21 is a photomicrograph, while the right-hand picture is a scanning electron micrograph (SEM). The left figure shows that all 20 emitters comprising the manifold

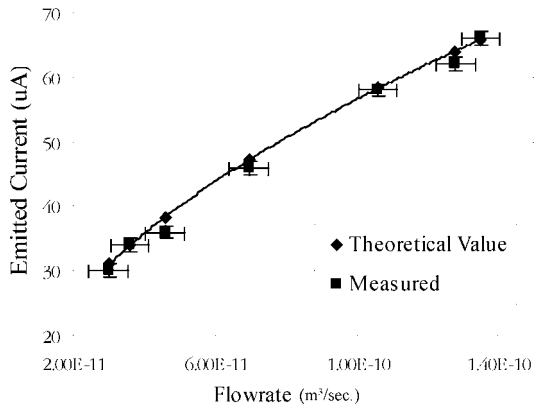

Fig. 22. Emitted current versus flowrate for a linear array fed with formamide. In this experiment, the electrical conductivity is equal to 0.612 S/m.

emitted droplets and deposited material on the collector. The right-hand figure shows that center-to-center distance between the deposited material is 130 μm, corresponding to the 130-μm pitch of the emitter design. The diameter of the deposits is 70 μm and fairly uniform. The imprints were obtained using NaI-doped formamide with an electrical conductivity equal to 2.9 S/m. With $K = 2.9$ S/m and the operation conditions, a semi-angle divergence equal to 8.06° is calculated using the reduced-order model by Lozano [6]. The SEM in Fig. 21 shows that the diameter of the imprints is 70 μm at a distance of 250 μm. A semi-angle divergence of 4° is estimated. The difference between the reduced order model and the experimental observation could be explained by the tendency of the reduced-order model to overestimate the semi-angle divergence, and the evaporation dynamics of the propellant after hitting the collector electrode [3]. The imprints are deposits of the propellant doping salt, left after the evaporation of the solvent—formamide. The doping concentration is about 30% by weight in the propellant used for this particular test. The relatively uniform imprints suggest uniform charge density inside the droplet fan and a sharp fan edge, consistent with the assertion that the plume has no thermalized tail.

E. Current–Flowrate Characteristics

Fig. 22 shows the experimental data of an engine using LiCl-doped formamide. The electrical conductivity of the propellant was estimated at 0.612 S/m. The figure plots experimental data as well as a model that assumes uniform emission from the arrays of emitters under steady-state single-Taylor-cone emission mode. The current was measured using a Hewlett-Packard micro voltammeter model 425 A. The flowrate was measured using a gas bubble. The error bars of the current measurements came from the current-meter specifications. The flowrate measurement error bars came from using Gauss' error propagation law on the equation that gives the flowrate Q

$$Q = \frac{L \cdot \pi \cdot D^2}{4 \cdot t} \tag{14}$$

where L is the length that the bubbles travels, D is the internal diameter of the tube, and t is the time it takes for the bubble to travel the length L.

V. Discussion

We have experimental evidence that suggests that the starting of a Taylor cone is not a clean process, especially if the meniscus does not have a well-defined wetting front [3]. Lowly doped propellants wet well the engine interior (propellant electrical conductivity smaller than about 0.3 S/m); unfortunately, the use of lowly doped propellants could make the engine work outside the region where electrical control is feasible. On the other hand, highly doped propellants do not wet well the engine interior (propellant electrical conductivity larger than about 1 S/m). Also, the external surface of the spouts is hydrophilic due to its roughness from plasma processing, and this condition is not corrected satisfactorily by the Teflon coating. We measured the wetting angle of doped formamide ($K = 2.9$ S/m) on bare silicon and on a silicon wafer covered with a 0.1-μm-thick Teflon coating using a Ramé-hart contact angle goniometer model 100. The Teflon coating came from running for 10 min the passivation cycle of the DRIE process. We obtained 10.0° of contact angle for the bare silicon sample and 88.5° for the Teflon-coated sample. Therefore, even though the Teflon coating should substantially reduce the wettability of the propellant on the emitter exterior, we speculate that the Teflon coating does not fill in the spout roughness enough to satisfactorily improve its nonwetting properties. The excessive emission of propellant during the Taylor cone start-up can make the engine generate transient arcs or sparks while in operation, possibly due to the large vapor pressure in the gap between the emitters and the electrodes. This is a serious issue that must be solved. The authors suggest a gas phase treatment of the engine interior to change its wetting properties, while the exterior should be coated with a material that will not wet.

The start-up of a Taylor cone works far better if information about what is occurring at the emitter tips is fed back. For a single emitter, this can be done by inspection of the emitter tip to see if a good meniscus is formed; if that is the case, the emitter is energized and, after Taylor cone formation is achieved, the voltage bias can be reduced to obtain a stable configuration. The actual engine testing setup does not have a way to visually inspect the emitters. It is also important to define a good strategy to diagnose, based on one or few emitters, the behavior of the whole set. This could take the form of probes at the engine exit to diagnose the droplet fans and use that information to correct the engine operation.

Given the fact that these turn-on transients are present, it may be desirable to use a different substrate material for the electrodes to reduce the chance of a breakdown event by surface contamination. An ideal candidate would be amorphous silica. Another solution to this problem would be to cover the electrodes with a suitable large breakdown voltage dielectric film to reduce the possibility of arcing if the vacuum gap insulation momentarily collapses due to the excessive presence of propellant.

Another important issue that has not been addressed is the neutralization of the engine. In all tests, the engine was part of a closed circuit, and there was no need for neutralization. The engine should not use an external neutralizer to avoid power losses of the order of the propulsive power of the engine. A good strategy would be to operate the engine in a dc bipolar mode,

that is, to emit different polarities at the same time to reach on overall engine charge neutrality.

VI. Conclusion

A silicon-based micro-fabricated linear array of electrospray thrusters that used doped formamide as propellant and operates in the single-Taylor-cone emission mode has been reported. This paper demonstrated the feasibility of high clustering of the emitters. It also demonstrated cumulative uniform emission of the engine, and uniform-steady operation of the modular units—a set of electrospray emitters fed by the same manifold. Other demonstrations include small droplet divergence in qualitative agreement with reported values in the literature and a reduced-order model. The paper also reported novel micro-fabrication techniques used to implement the engine. On the downside, the paper also observed that the spouts of the linear array did not have a well-defined wetting front because of the inherent roughness of DRIE and the hydrophobic behavior of the engine interior with respect to doped formamide, causing the emission of propellant bursts in the startup process.

Acknowledgment

The authors would like to express their gratitude to the staff of MIT's Micro-fabrication Technologies Laboratory for their help on the fabrication of the linear array.

References

[1] G. I. Taylor, "Disintegration of water drops in an electric field," *Proc. R. Soc. London*, vol. A 280, no. 1382, pp. 383–397, 1964.
[2] S. P. Thompson and P. D. Prewett, "The dynamics of liquid metal ion sources," *J. Phys. D: Appl. Phys.*, vol. 17, pp. 2305–2321, 1984.
[3] L. F. Velásquez-García, "The design, fabrication and testing of micro-fabricated linear and planar colloid thruster arrays," Ph.D. dissertation, Dept. Aeronaut. Astronaut., Mass. Inst. Technol., Cambridge, 2004.
[4] J. de la Mora, "The current emitted by highly conductive taylor cones," *J. Fluid Mech.*, vol. 260, pp. 155–184, 1994.
[5] V. Hruby, "Micro Newton colloid thruster system development," in *Proc. 27th Int. Electric Propulsion Conf.*, Pasadena, CA, 2001, IEPC-01-281.
[6] P. Lozano, "Studies on the ion-droplet mixed regime in colloid thrusters," Ph.D. dissertation, Dep.t. Aeronaut. Astronaut, Mass. Inst. Technol., Cambridge, 2003.
[7] W. Kenneth, Research and Development in Needle and Slit Colloid Thrusters Goddard Space Flight Center, Greenbelt, MD, NASA TN D-5305, 1969.
[8] H. Daley, "Experimental study of colloid annular thrusters," in *Proc. 8th AIAA Electric Propulsion Conf.*, Stanford, CA, 1970, AIAA-1970-1112.
[9] ——, "Colloidal annular array thruster development," in *Proc. AIAA 10th Electric Propulsion Conf.*, Lake Tahoe, NV, 1973, 73A1077.
[10] J. Fenn, "Colloid ionization for mass spectrometry of large biomolecules," *Science*, vol. 246, pp. 64–71, 1989.
[11] J. Mueller, "Thruster options for microspacecraft: A review and evaluation of existing hardware and emerging technologies," in *Proc. 33rd AIAA/ASME/SAE/ASEE Joint Propulsion Conf. Exhibit*, Seattle, WA, 1997, AIAA 1997-3058.
[12] M. Paine, "A micro-fabricated colloid thruster array," in *Proc. 37th AIAA/ASME/SAE/ ASEE Joint Propulsion Conf. Exhibit*, Salt Lake City, UT, 2001, AIAA 2001-3329.
[13] J. Xiong, "The designing, fabrication and test of a MEMS-based micro-colloid thruster," *Proc. SPIE*, vol. 4928–24, 2002.
[14] ——, "A colloid microthruster system," *Microelectron. Eng.*, vol. 61–62, pp. 1031–1037, 2002.
[15] G. Schultz, T. N. Corso, S. J. Prosser, and S. Zhang, "A fully integrated monolithic microchip electrospray device for mass spectrometry," *Anal. Chem.*, vol. 72, pp. 4058–4063, 2000.
[16] M. Paine, "Design study for micro-fabricated colloidal thrust," M.S. thesis, Dept. Aeronaut. Astronaut., Mass. Inst. Technol., Cambridge, 1999.
[17] L. F. Velásquez, "Advances in micro-fabricated droplet emission mode 1D colloid thruster array," in *Proc. Space Propulsion 2004, Electric Propulsion Systems Session*, Sardinia, Italy, 2004.
[18] ——, "Two-dimensional micro-fabricated colloid thruster array," in *Proc. 40th Joint AIAA/ASME/SAE Propulsion Conf.*, Fort Lauderdale, FL, 2004, AIAA-2004-3595.
[19] L. F. Velásquez, A. I. Akinwande, and M. Martinez-Sanchez, "Precision hand assembly of MEMS subsystems using meso-scaled DRIE-patterned deflection spring structures: An example with out-of-plane wafer assembly," *J. Microelectromech. Syst.*, submitted for publication.
[20] H. Jansen, "The black silicon method: A universal method for determining the parametric setting of a fluorine-based reactive ion etcher in deep silicon trench etching with profile control," *J. Micromech. Microeng.*, vol. 5, no. 2, pp. 115–20, Jun. 1995.
[21] M. Gamero, "Colloid as a source of nanoparticles for efficient colloid thrusters," *J. Propulsion Power*, vol. 17, no. 5, pp. 115–20, 2001.

Luis Fernando Velásquez-García received the Mechanical Engineer degree (*magna cum laude*) and the Civil Engineer degree (*magna cum laude*) from Los Andes University, Bogotá, Colombia, in 1998 and 1999, respectively, and the M.S. degree in aeronautics and astronautics and the Ph.D. degree in space propulsion from the Massachusetts Institute of Technology (MIT), Cambridge, in 2001 and 2004, respectively.

After completing his studies, he became a Postdoctoral Associate (2004) affiliated with the MIT's Microsystems Technology Laboratories (MTL), and the Gas Turbine Laboratory (GTL). Since 2005, he has held an appointment as Research Scientist, affiliated with the same laboratories at MIT. His research focuses on micro– and nano–fabrication technologies applied to propulsion, structures, and power systems. He has conducted research in micro- and nano-technology applied to electrospray arrays, mass spectrometry, field emission, mass/charge sensors, 3-D packaging, electron impact ionization, field ionization, plasma–enhanced chemical vapor deposition, carbon nano-tube–based devices, turbomachinery, and chemical lasers.

Akintunde Ibitayo Akinwande (M'00) received the B.Sc. degree in electrical and electronic engineering from the University of Ife, Ife, Nigeria, in 1978, and the M.S. and Ph.D. degrees in electrical engineering from Stanford University, Stanford, CA, in 1981 and 1986, respectively.

He joined the Honeywell Technology Center, Bloomington, MN, in 1986, where he initially conducted research on GaAs complementary FET technology for very-high-speed signal processing. He later joined the Si Microstructures Group, where he conducted research on pressure sensors, accelerometers, thin-film field emission, and display devices. He joined the Microsystems Technologies Laboratories, Massachusetts Institute of Technology (MIT), Cambridge, in 1995, where his research focuses on device and micro-fabrication technologies with particular emphasis on smart displays, large-area electronics, field emission and field ionization devices, and electric propulsion. He is currently a Professor in MIT's Electrical Engineering and Computer Science Department. He holds four patents in MEMS and display technologies and has authored more than 50 journal publications.

Prof. Akinwande is a recipient of the 1996 National Science Foundation Career Award. He has served on a number of technical program committees for various conferences, including the Device Research Conference, the International Electron Devices Meeting, the International Solid-State Circuits Conference, the International Display Research Conference, and the International Vacuum Microelectronics Conference.

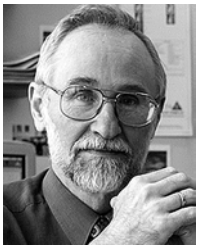

Manuel Martínez-Sánchez received the Aeronautical Engineer's degree from the Polytechnic University of Madrid, Madrid, Spain, in 1967, and the Ph.D. degree from the Massachusetts Institute of Technology (MIT), Cambridge, in 1973.

His professional career has been entirely as a teacher at MIT, where he is currently a Professor of Aeronautics and Astronautics. His research and teaching are concentrated on space propulsion, after having in the past looked into MHD power generation and other energy-related topics. He is currently director of the MIT Space Propulsion Laboratory, where theoretical and experimental research is being conducted on plasma thrusters, thruster plumes, and micro-propulsion using electrospray phenomena. He has authored about 30 journal papers and 120 conference papers.

Prof. Martínez-Sánchez is a Corresponding Member of the Spanish Academy of Engineering.